Caldera Collapse Geometry Revealed by Near-field GPS Displacements at Kīlauea Volcano in 2018

Paul Segall[1], Kyle R. Anderson[2], Fabio Pulvirenti[3], Taiyi Wang[1], Ingrid Johanson[4]

[1]Geophysics, Stanford University
[2]U.S. Geological Survey, California Volcano Observatory
[3]Jet Propulsion Laboratory, Caltech
[4]U.S. Geological Survey, Hawaiian Volcano Observatory

Key Points:

- Discrete collapse events exhibit radial outward displacements up to 20 cm and uplift of over 5 cm outside caldera
- Data best fit by slip on normal ring-fault that steepens with depth and associated pressurization of underlying magma chamber
- Triaxial point source fits the data well, but yields a strongly biased estimate of the source depth and kinematics

Corresponding author: Paul Segall, `segall@stanford.edu`

Abstract

We employ near-field GPS data to determine the subsurface geometry of a collapsing caldera during the 2018 Kīlauea eruption. Collapse occurred in 62 discrete events, with "inflationary" deformation external to the collapse, similar to previous basaltic collapses. We take advantage of GPS data from the collapsing block, and independent constraints on the magma chamber geometry from inversion of deflation prior to collapse onset. This provides an unparalleled opportunity to constrain the collapse geometry. Employing an axi-symmetric finite element model, the co-collapse displacements are best explained by piston-like subsidence along a high angle ($\sim 85°$) normal ring-fault that may steepen to vertical with depth. Reservoir magma has compressibility of $2 \rightarrow 15 \times 10^{-10}$ Pa^{-1}, indicating bubble volume fractions from 1 to 7 % (lower if fault steepens with depth). Magma pressure increases during collapses are 1 to 3 MPa, depending on compressibility. A tri-axial point source in a homogeneous half-space fits the data well, but provides a biased representation of the source depth and process.

Plain Language Summary

When large volumes of magma erupt rapidly the rock overlying the subsurface reservoir founders producing a caldera. During the 2018 eruption of Kilauea volcano, Hawaii collapse occurred in over 60 events, each lasting 5 to 10 seconds. We analyze GPS data collected during the last 32 of these events to determine the geometry of the ring fault system bounding the caldera block and the properties of the underlying magma. The faults are on average very steep, but slightly inward dipping at shallow depth. Inferred pressure increases during collapse events constrain the compressibility of the magma and imply an exsolved gas phase with from 1 to 7 % bubbles by volume.

1 Introduction

The largest volcanic eruptions are accompanied by caldera collapse. While caldera formation is understood to result from the rapid withdrawal of large volumes of magmas from crustal reservoirs, the geometry of these reservoirs and in particular the dip of the ring-fault systems (normal vs reverse) are not well understood. Constraints come from geologic observations of eroded calderas, geophysical observations, as well as analog and numerical modeling (*Cole et al.*, 2005; *Branney and Acocella*, 2015). Caldera collapses are thankfully rare and relatively little data has been collected in the near field of an ongoing collapse.

Historic caldera collapses at basaltic shield volcanoes occur in discrete events; the Kīlauea 2018 eruption consisted of 62 such collapse events (*Neal et al.*, 2019; *Tepp et al.*, 2020). These events were accompanied by very long period (VLP) earthquakes and remarkable "inflationary" deformation (Figure 1). Similar behavior was observed at Miyake-jima, Japan and Piton de la Fournaise on Reunion Island (*Kumagai et al.*, 2001; *Michon et al.*, 2009). Kīlauea high rate GPS data show that the collapse events took place over 5 to 10 seconds. During this time negligible magma could have left the underlying chamber, meaning that collapses occurred under constant mass conditions. *Segall et al.* (2019) showed that under these conditions co-collapse deformation results from a combination of chamber pressurization and fault slip. For a vertical ring-fault the deformation external to the collapse is caused solely by pressure increase in the chamber; for other dips fault-induced deformation contributes to surface displacements and tilts.

The eruption of Kīlauea in 2018 provided unique data during a caldera collapse (*Neal et al.*, 2019; *Anderson et al.*, 2019; *Tepp et al.*, 2020). The eruption began on May 3, 2018 in the lower East Rift Zone (ERZ). Deflation at Kīlauea's summit began the previous day and accelerated following a M 6.9 south flank earthquake on May 4. On May 16 the first rapid inflation event occurred contemporaneous with significant ash emission. By May 29 fault-bounded collapse was evident outside of Halema'uma'u crater. Later in the eruption collapse events were accompanied by higher effusion rates at the eruption site (*Patrick et al.*, 2019). During June a new surface fault scarp propagated clockwise through the existing (1500 CE) Kīlauea caldera, establishing a roughly circular collapse structure by mid to late June 2018. The floor of Halema'uma'u crater ultimately dropped up to 500 meters and the volume of the caldera increased by ~ 0.8 km^3.

Here we build on the conceptual modeling of *Segall et al.* (2019); specifically, we use near-field GPS data to constrain collapse structure at depth. We develop a forward model conditioned on observations prior to collapse onset. Unknown parameters are constrained by near-field, co-collapse GPS displacements. To contrast with point source models commonly employed in volcano deformation studies, we compare results with inversions based on a tri-axial point source in a homogeneous half-space. The point source has more degrees of freedom than the finite element method (FEM) based model, and is not restricted to radial symmetry. Nevertheless, it cannot capture the kinematics of the collapse and could lead to biased interpretations.

2 Method

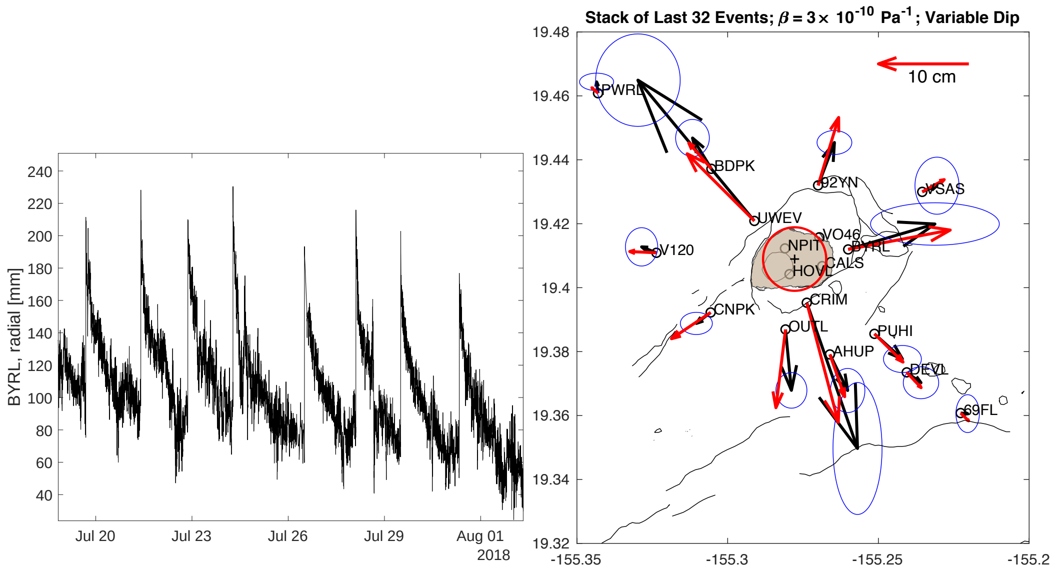

Figure 1. A) Time series of radial component GPS displacements at BYRL. Positive displacement indicates motion away from the caldera. Station location shown in B. B) Co-collapse radial displacements. Black: average of last 32 collapse events, with 95% confidence ellipses reflecting the variability of the individual events. Red: predicted by model with fault dip increasing from 85° to vertical at 600 m (see Figure 2) and magma compressibility $\beta_m = 3\times10^{-10}$ Pa^{-1}. Collapse structure is shaded. Red circle shows location of model ring-fault. Scale vector is 0.1 m.

We analyze high rate GPS data (5 second sampling) from collapse events later in the eruption, after the eastern section of the ring-fault system was fully formed. A sample time series for station BYRL is shown in Figure 1a. The co-collapse displacement in individual events was determined as the difference between pre- and post event positions averaged over 5 minutes, not including a window ±1 minute around the time of the event. We then computed the mean and variance of the co-collapse displacements for the last 32 events. We find that stations closest to the collapse have more variability and are thus down-weighted relative to more distant stations in our inversions. An alternate approach is to stack time series at each station (last 32 events), and then compute co-collapse displacements from the stack. Uncertainties in this case are computed by taking the standard deviation of samples in the 4-minute pre- and post-collapse windows and propagating these uncertainties into the offset, assuming they are uncorrelated and normally distributed. While these two approaches lead to essentially identical displacements stacking results in substantially smaller but more uniform uncertainties. For completeness we present results with both sets of weights.

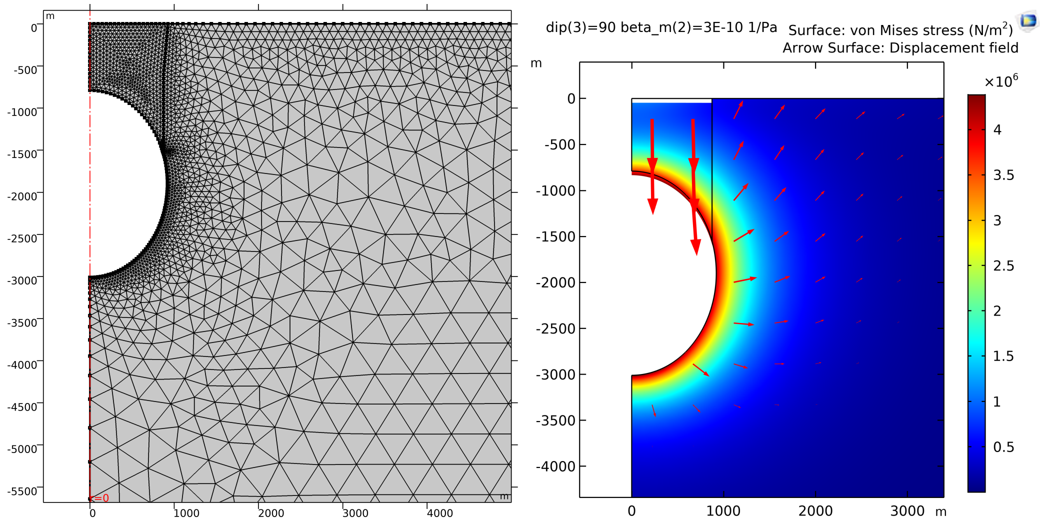

Figure 2. A) Finite element mesh showing the magma chamber and an inward dipping fault that steepens with depth. Geometry is radially symmetric about the red dashed line. B) Maximum shear (von Mises) stress for vertical ring-fault. Vectors represent displacements with log scaling to permit viewing of displacements outside the collapse piston. Note that stresses are due solely to chamber pressurization.

We take advantage of constraints on the magma chamber geometry inferred from analysis of pre-collapse deflation measured by GPS, tilt, and InSAR (*Anderson et al.*, 2019). We take the median values for the chamber parameters to construct a radially symmetric FEM model of a typical collapse event (Figure 2). The model consists of an ellipsoidal reservoir and a ring-fault from the surface to the magma chamber. Of course, neither the collapse geometry nor displacements are radially symmetric (Figure 1b). Rather, the collapse occured on pre-existing faults along much of the south and west margins, whereas a new (at least at a the surface) intra-caldera fault developed along the east margin of the 2018 collapse. High frequency (volcano tectonic, VT) seismicity was concentred along this new structure (*Shelly and Thelen*, 2019).

From *Anderson et al.* (2019) (see Supplemental Information) the median magma chamber has initial volume $V = 3.9$ km^3, and centroid depth 1.9 km, whose apex reaches to ~ 0.8 km below the surface (Figure 2). Note that the pre-collapse model places only first-order constraints on the shape of and depth to the top of the reservoir. The average vertical displacement during the last 32 collapse events, from GPS station CALS located on the down-dropped block (Figure 1b) was $\sim$ 2.5 meters. Thus, fault slip, assumed for simplicity to be uniform along the ring-fault, is taken as $2.5/\sin(\delta)$ meters, where δ is fault dip.

The surface deformation during collapse events depends on the geometry of the magma chamber and ring-fault system, and the pressure change induced by reduction in chamber volume due to downward motion of the roof block. As shown in Supplemental Information, the co-collapse displacements $u_{\rm co}(\mathbf{x})$ at radial position $\mathbf{x}$ are

$$u_{\rm co}(\mathbf{x}) = s\left[\frac{-\Phi(\mathbf{m},\delta)f(\mathbf{x};\mathbf{m})}{\mu\,(\beta_m+\beta_c)} + g(\mathbf{x};\mathbf{m},\delta)\right]. \qquad (1)$$

Here s is fault slip, $f(\mathbf{x};\mathbf{m})$ is function of model parameters $\mathbf{m}$ that characterize the chamber (depth to centroid, vertical and horizontal semi-axes); $g(\mathbf{x};\mathbf{m},\delta)$ is a dimensionless function that maps slip to displacement at constant chamber pressure. Further, $\Phi \equiv \partial V/\partial s$ at constant p. Finally, μ is the crustal shear modulus, β_m and $\beta_c \equiv (1/V)\partial V/\partial p$ are the magma and chamber compressibilities. The latter depends on μ and chamber geometry. Note Φf and $\mu\,(\beta_m+\beta_c)$ are dimensionless.

The average elastic properties of the crust are imperfectly known, but are chosen to be consistent with the pre-collapse modeling. The surface expression of the ring-fault is constrained by direct observation and roughly coincides with the inferred outline of the magma chamber (*Anderson et al.*, 2019). By fixing the geometry (including V) and μ, which determines both β_c and Φ to that estimated from pre-collapse data, the only unknown parameters are fault dip and magma compressibility. We search over $(\delta,\ \beta_m)$ space to determine parameters that optimize fit to the co-collapse data.

Equation (1) is important for understanding how the data scale with mechanical and geometric parameters. As described in the SI, the pressure change in the first term does not appear explicitly. However, in the FEM calculations $\Delta p_{\rm co}$ induced by collapse is computed by

$$\Delta p_{\text{co}} = -\frac{\Delta V}{V\beta_m}, \tag{2}$$

where ΔV is the change in chamber volume.

We use the finite element code COMSOL Multiphysics to determine the surface deformation due to fault slip on a ring-fault coupled to a magma chamber (Figure 2). Slip is spatially uniform and imposed on the ring-fault. Displacement of the plug into the chamber reduces its volume, increasing magma pressure according to equation (2). This spatially uniform pressure change and zero shear traction provide the boundary condition on the walls of the chamber. The model domain dimensions are 20x the largest dimension of the chamber, sufficient to avoid boundary effects; results are insensitive to mesh refinement. We search over a range of fault dips and magma compressibilities and compare to the observed displacements.

3 Results

Figure 3 shows misfit, defined as the weighted residual 2-norm, including vertical and radial displacements, as a function of dip and compressibility. Figure 3a shows results with weights determined by the variance of the events, while Figure 3b employs the lower variance determined by first stacking the last 32 events. In both cases it is clear that a (normal) dip of 85° fits the data best over a range of compressibilities, with optimal values of β_m of 15 and 7 $\times 10^{-10}$ Pa^{-1}, respectively. Vertical ring-faults with $\beta_m = 1 \rightarrow 3 \times 10^{-10}$ Pa^{-1} also fit the data with larger errors reasonably well (Fig. 3a). Shallower normal faults ($\delta \leq 85°$) and reverse faults ($\delta = 95°$) generally do not fit the data well.

Figure 4a,b compare radial and vertical displacements as a function of distance from the collapse center with predictions from the FEM model for the optimal magma compressibility, $\beta_m = 7 \times 10^{-10}$ Pa^{-1}, and a range of ring-fault dips. The 85° dipping ring-fault fits data quite well, although under-predicting the radial displacements of the nearest stations (CRIM and UWEV). As noted by *Segall et al.* (2019), outward dips ($> 90°$) result in inward directed (negative) displacements close to the collapse, contrary to observations. This is most pronounced with compressible magmas because of the smaller pressure change (Figure 3c), which increases the relative contribution of the ring-fault to the surface deformation. With less compressible magmas (see SI) the predicted ra-

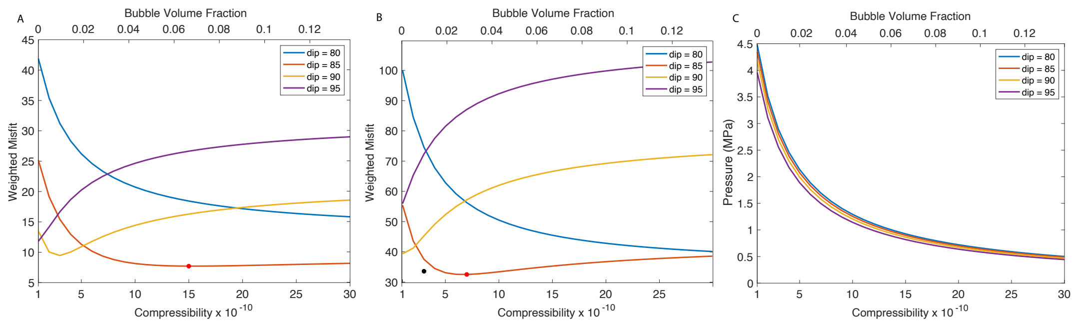

Figure 3. Weighted residual norm as a function of fault dip and magma compressibility. Red star indicates minimum misfit. Top axis gives the implied bubble volume fraction (see Discussion). a) Standard deviation determined from the 32 separate events. b) Standard deviation determined from stack of events. Black star indicates misfit for fault with variable dip. c) Computed pressure change in the magma chamber.

dial displacements are outward, but decrease as the ring-fault is approached, contrary to the data (SI Fig. 1). These observations exclude an outward dipping ring-fault. With the compressibility of gas free basalt, the minimum reasonable value, $\beta_m \sim 1{\times}10^{-10}$ Pa^{-1}, the model over predicts the vertical displacements for all dips (SI). As described in the Discussion, these results imply the presence of an exsolved vapor phase in the magma chamber.

Figure 4c,d illustrates results for $\beta_m = 3 \times 10^{-10}$ Pa^{-1}, near the local minimum in misfit for a vertical ring-fault (Fig. 3a). For this compressibility, the vertical ring-fault fits the radial displacements well at more distant stations (Fig. 4c), but significantly underpredicts the radial displacements at the closer stations. While the 85° dipping fault better fits the close-in radial displacements, it over predicts both the more distant stations as well as the vertical displacements. This suggests that the ring-fault may steepen with depth, which we tested for a number of scenarios. Figure 4c,d shows the prediction for a ring-fault that dips 85° at the surface and steepens to vertical at 600 m depth (Fig. 2a). As expected, this fits the radial displacements at the more distant stations and does a better job of fitting the closer stations. It over predicts the vertical displacements, but generally fits the data within one standard deviation. Dips that steepen with depth are consistent with field observations that show inward (normal) dips at the surface. (The ratio of vertical to horizontal displacements at CALS (see Fig. 1b) indicate a dip at the earth's surface of 71.5°).

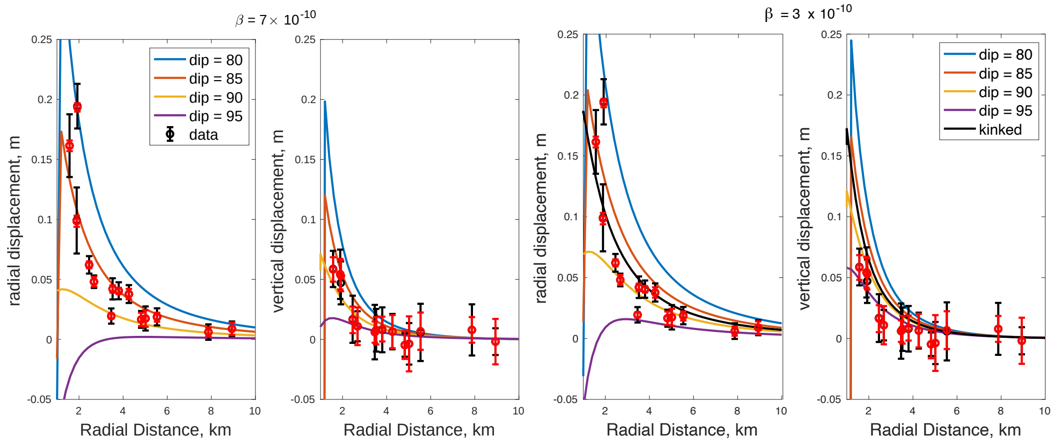

Figure 4. Predicted and observed radial (a,c) and vertical (b,d) displacements during a collapse event. 1-sigma error bars; simple averaging (black) and stacking (red). Predictions are shown for a range of dips (dips less than 90° are normal faults) and $\beta_m = 7 \times 10^{-10}$ Pa^{-1} (a,b) and for $\beta_m = 3 \times 10^{-10}$ Pa^{-1} (c,d). Also shown is the case with fault dip that steepens from 85° to vertical at a depth of 600m, labeled "kinked".

The fit to the horizontal displacements of the steepening fault model is shown in Figure 1b. The model under predicts the displacement at UWEV and over predicts the displacements at CNPK and 92YN, a consequence of the assumed radial symmetry. Some aspect of the ring-fault chamber system led to larger displacements in the northwestern direction at UWEV, although BDPK is fit well, suggesting this feature is shallow. One possibility is a locally shallower dip along this section of the ring-fault. It is also possible that there is some asymmetry in the shallow magma reservoir, although asymmetry in the pre-collapse deformation was small (*Anderson et al.*, 2019). Given the symmetry of the forward model and the fact that only two parameters are adjusted, the fit is reasonable.

The pressure increase during a typical collapse event is shown in Figure 3c. Because the slip amplitude is specified, less compressible magmas result in larger pressure increases (equation 2). Fault dip has a minor effect with normal faulting giving slightly larger pressure increases. Given the range of parameters that fit the data, our results suggest that pressure increases ranged from 3.3 MPa (for a vertical ring-fault and a compressibility of 2×10^{-10} Pa^{-1}) to 1.25 MPa (for an 85° dip and compressibility of 10^{-9} Pa^{-1}.)

4 Discussion

The compressibility of gas-free basalt is $\beta_l \sim 1\times10^{-10}$ Pa^{-1} (*Murase and McBirney*, 1973; *Spera*, 2000). Our results suggest the compressibility of magma in the Halema'uma'u reservoir is $\beta_m = 2 \to 15 \times 10^{-10}$ Pa^{-1}, implying an exsolved gas phase. The magma compressibility can be expressed in terms of the volume fraction of gas phase ϕ,

$$\beta_m \quad = \quad (1-\phi)\beta_l + \phi\beta_g = (1-\phi)\beta_l + \phi/p, \tag{3}$$

where the gas is assumed to be ideal. Taking the pressure to be magmastatic at the chamber centroid depth, with density 2.5×10^3 implies vesicularities of ϕ of 0.01 to 0.07, and possibly as high as 0.12 (Fig. 3). Given that bubbles rise rapidly in low viscosity basalt, high *in situ* gas volume fractions may be unrealistic, however it is beyond our scope to bound plausible values. It also should be noted from equation (1) that displacements depend on the product of shear modulus μ and total compressibility. It is possible that the effective shear modulus for short-duration collapse events may have been greater than that for weeks-long deflation. If so, this could be consistent with lower compressibility and vesicularity.

We used the ~ 2.5 m rapid downward displacement of CALS (Figure 1b) to measure sudden collapse in a typical event. CALS also experienced ~ 2 m slow subsidence between collapse events. This may reflect fault creep, perhaps localized along the newer, eastern sector of the ring-fault associated with abundant VT seismicity (*Shelly and Thelen*, 2019). Because CALS is close to the eastern ring-fault, it is possible that it is unrepresentative of the collapse as a whole. If the main collapse experienced the cumulative displacement at CALS it would have been closer to 4.5 meters.

The cumulative displacements recorded from repeated digital elevation models (DEM) provide another estimate of the vertical drop in an average collapse. Between July 13 and the end of the eruption the eastern block subsided about 60-70 m, in 13 events, or ~ 5 meters per event. However, this does not determine how much was slow inter-event subsidence. We find that solutions with 5 meters of slip do not fit as well, especially at the closest stations, and favor vertical ring-faults. Because the slow inter-event displacement at CALS coincides with VT seismicity, we favor the interpretation that vertical displacement per event is closer to 2.5 m, but with only one site on the down-dropped block we cannot rule out up to 5 m of collapse.

Our calculations have not accounted for the Overlook vent, or topographic effects of the pre-existing (1500 CE) caldera or newly formed collapse pit as it was expressed in mid June, 2018 at the start of the data analyzed here. Forward models including a conical "pit" with radius 700 m and depth up to 300 m did not significantly alter the conclusions presented here. The pit has greatest effect on horizontal displacements, particularly with the reverse ring-fault geometry. Deeper pits and significant disk-shaped calderas have more significant effects. Full three dimensional modeling with accurate surface topography is beyond our scope, but appears unlikely to fundamentally alter our conclusions.

The results above fix the magma chamber geometry to the median values determined from analysis of pre-collapse deflation. To explore the effects of uncertainty in chamber geometry on inferred properties, we resample from the posterior distribution of *Anderson et al.* (2019). For a vertical ring-fault the surface deformation outside the collapse is simply rigid body translation of the piston plus pressurization of the chamber (*Segall et al.*, 2019) (see also below). Thus, we can employ the model emulator developed by *Anderson et al.* (2019) to predict the surface deformation due to a co-collapse pressure increase. Least squares estimation of pressure change Δp_{co} given by equation (2), assuming 2.5 m subsidence per event, along with other parameters are shown in the Supplemental Information (SI Fig. 2).Δp_{co} is normally distributed with a mean of 3 MPa and standard deviation of 0.3 MPa. The inferred magma compressibility ranges from roughly 3×10^{-10} to 2×10^{-9} Pa^{-1}. While this range is for vertical ring-faults it may reasonably approximate normal faults that steepen to vertical at shallow depth.

Volcano deformation studies often model source processes with point source approximations of magma chambers. To contrast this with the finite source model above, we invert the co-collapse displacements for a tri-axial point-source. A single point source necessarily combines the contributions of the ring-fault and the magma chamber in a single source, although the true source is distributed in depth. We follow the procedure of *Davis* (1986) see also *Segall* (2010, Chapter 7), using Green's tensors for a homogeneous half-space, but do not associate the double forces in terms of a pressure boundary condition on a spheroidal magma chamber. We restrict one double force to vertical; relaxing this improves the fit somewhat, but does not alter the interpretation. We estimate the source location and the best-fitting moment tensor with a Markov Chain Monte Carlo (MCMC) procedure.

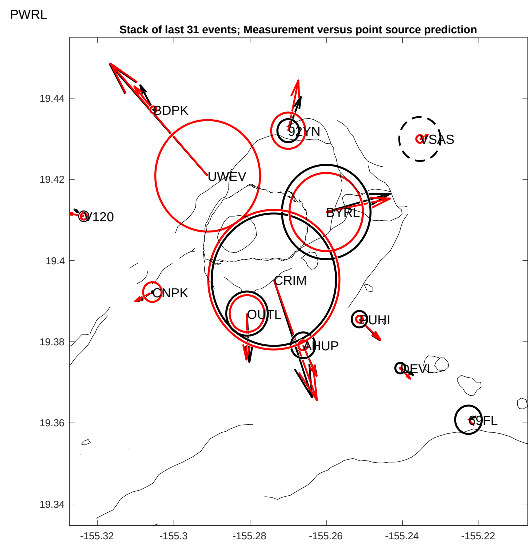

Figure 5. Comparison of observed co-collapse displacements (black) with those predicted by a generalized point-source moment tensor in an elastic half-space (red). Circles represent vertical displacements, dashed where negative.

The point source model fits the data quite well (Figure 5). Posterior distributions for the point-source parameters are given in the SI (SI Fig. 3). The median source depth is $\sim$ 700 m, much shallower than the chamber centroid inferred from pre-collapse data (*Anderson et al.*, 2019). While the point source combines contributions from the ring-fault and magma chamber, which are at different depths, it should be dominated by the chamber for near vertical ring-faults. Thus, the source depth is unrealistically shallow. The best fitting source is largely isotropic expansion (SI Fig. 4) with minor CLVD and double couple components. The vertical double-force is maximum; the largest horizontal double-force is directed NW/SE reflecting the displacements at UWEV and CRIM (Figure 9b) compared to the orthogonal NE/SW direction.

An expansion source might seem counterintuitive for a collapsing caldera, because the "inflationary" deformation observed outside the collapse structure is caused by a volume *decrease* but a pressure *increase*. Consider the case of a vertical ring-fault: Due to linearity in the problem the forward model can be decomposed into: 1) displacement of the piston into a magma chamber at constant pressure, and 2) the pressurization of the chamber due to the resulting volume decrease. The first step is a rigid body motion and produces no deformation outside the piston. Thus, for a vertical ring-fault the pressure increase is the sole cause of deformation external to the caldera. This indicates that there should be some caution in interpreting moment tensor estimates for volumetric sources in terms of source kinematics. We also explored forcing the point source to be located at the *a priori* chamber centroid depth. Not surprisingly, fit to the co-collapse displacements is degraded; in particular, the vertical displacements are significantly over-predicted.

As noted above, the collapse faults are normal at the surface, while the geodetic data are consistent with dips steepening with depth. In contrast, many analog and numerical models (*Acocella*, 2007; *Ruch et al.*, 2012; *Holohan et al.*, 2011; *Geyer and Martí*, 2014) find initial development of an inner reverse ring-fault with subsequent growth of a peripheral fault that may have a normal geometry. In contrast to these studies, the Kīlauea collapse was clearly influenced by the presence of the lava lake, Halema'uma'u crater, and pre-existing caldera bounding structures. In particular, the presence of the lava lake conduit seems to have promoted inward slumping. Another factor favoring normal faulting is regional extension (*Acocella*, 2007), which is present at Kīlauea due to seaward motion of the volcano's south flank (*Owen et al.*, 2000; *Denlinger and Morgan*, 2014).

5 Conclusions

- Collapse events were accompanied by remarkable "inflationary" deformation external to the caldera with radial outward displacements of nearly 20 cm and uplift of over 5 cm.
- For a constant fault dip the data are best fit by a steeply dipping (85°) normal ring-fault with a magma estimated to have on the order of 3% bubble volume fraction.
- For lower bubble volume fractions, fit to the stations closest to the caldera is improved if the fault dip increases from roughly 85° to vertical at a depth of ~ 600 meters, qualitatively consistent with normal faulting observed at the surface.
- Estimates of pressure increases during collapse events range from 1 to over 3 MPa, depending on magma compressibility. Uncertainty in magma chamber volume alone introduces an uncertainty in pressure change on the order of 0.3 MPa.
- A generalized triaxial point source can fit the data quite well, but yields a strongly biased estimate of the source depth and kinematics.

Acknowledgments

Thanks to Gary Mavko for discussion. GPS data are available from the UNAVCO archive: https://www.unavco.org/data/data.html

References

Acocella, V. (2007), Understanding caldera structure and development: An overview of analogue models compared to natural calderas, *Earth-Science Reviews*, *85*(3-4), 125–160.

Anderson, K. R., I. A. Johanson, M. R. Patrick, M. Gu, P. Segall, M. P. Poland, E. K. Montgomery-Brown, and A. Miklius (2019), Magma reservoir failure and the onset of caldera collapse at kīlauea volcano in 2018, *Science*, *366*(6470).

Branney, A., and V. Acocella (2015), Calderas, in *The encyclopedia of volcanoes*, edited by H. Sigurdsson, pp. 299–315, Elsevier.

Cole, J., D. Milner, and K. Spinks (2005), Calderas and caldera structures: a review, *Earth-Science Reviews*, *69*(1-2), 1–26.

Davis, P. M. (1986), Surface deformation due to inflation of an arbitrarily oriented triaxial ellipsoidal cavity in an elastic half-space, with reference to kilauea volcano, hawaii, *Journal of Geophysical Research: Solid Earth*, *91*(B7), 7429–7438.

Denlinger, R. P., and J. K. Morgan (2014), Instability of Hawaiian volcanoes, *Characteristics of Hawaiian volcanoes*, *1801*, 149–176.

Geyer, A., and J. Martí (2014), A short review of our current understanding of the development of ring faults during collapse caldera formation, *Frontiers in Earth Science*, *2*, 22.

Holohan, E., M. Schöpfer, and J. Walsh (2011), Mechanical and geometric controls on the structural evolution of pit crater and caldera subsidence, *Journal of Geophysical Research: Solid Earth*, *116*(B7).

Kumagai, H., T. Ohminato, M. Nakano, M. Ooi, A. Kubo, H. Inoue, and J. Oikawa (2001), Very-long-period seismic signals and caldera formation at Miyake island, Japan, *Science*, *293*(5530), 687–690.

Michon, L., N. Villeneuve, T. Catry, and O. Merle (2009), How summit calderas collapse on basaltic volcanoes: New insights from the april 2007 caldera collapse of Piton de la Fournaise volcano, *Journal of Volcanology and Geothermal Research*, *184*(1-2), 138–151.

Murase, T., and A. R. McBirney (1973), Properties of some common igneous rocks and their melts at high temperatures, *Geological Society of America Bulletin*, *84*(11), 3563–3592.

Neal, C., S. Brantley, L. Antolik, J. Babb, M. Burgess, K. Calles, M. Cappos, J. Chang, S. Conway, L. Desmither, et al. (2019), The 2018 rift eruption and summit collapse of Kīlauea volcano, *Science*, *363*(6425), 367–374.

Owen, S., P. Segall, M. Lisowski, A. Miklius, R. Denlinger, and M. Sako (2000), Rapid deformation of Kilauea volcano: Global positioning system measurements between 1990 and 1996, *J. Geophys. Res.*, *105*(B8), 18,983 – 18,998.

Patrick, M., H. Dietterich, J. Lyons, A. Diefenbach, C. Parcheta, K. Anderson, A. Namiki, I. Sumita, B. Shiro, and J. Kauahikaua (2019), Cyclic lava effusion during the 2018 eruption of kīlauea volcano, *Science*, *366*(6470).

Ruch, J., V. Acocella, N. Geshi, A. Nobile, and F. Corbi (2012), Kinematic analysis of vertical collapse on volcanoes using experimental models time series, *Journal of Geophysical Research: Solid Earth*, *117*(B7).

Segall, P. (2010), *Earthquake and Volcano Deformation*, 432 pp., Princeton Univ. Press.

Segall, P., K. R. Anderson, I. Johanson, and A. Miklius (2019), Mechanics of inflationary deformation during caldera collapse: Evidence from the 2018 kı¯ lauea eruption, *Geophysical Research Letters*.

Shelly, D. R., and W. A. Thelen (2019), Anatomy of a caldera collapse: Kīlauea 2018 summit seismicity sequence in high resolution, *Geophysical Research Letters*.

Shuler, A., G. Ekström, and M. Nettles (2013), Physical mechanisms for vertical-clvd earthquakes at active volcanoes, *Journal of Geophysical Research: Solid Earth*, *118*(4), 1569–1586.

Spera, F. (2000), Physical properties of magma, in *Encyclopedia of Volcanoes*, edited by H. Sigurdsson, pp. 171–190, Academic Press, San Diego, CA, USA.

Tepp, G., A. Hotovec-Ellis, B. Shiro, I. Johanson, W. Thelen, and M. M. Haney (2020), Seismic and geodetic progression of the 2018 summit caldera collapse of kīlauea volcano, *Earth and Planetary Science Letters*, *540*, 116,250.